Estimates of stress drop and crustal tectonic stress from the 27 February 2010 Maule, Chile, earthquake: Implications for fault strength

Karen M. Luttrell,[1,2] Xiaopeng Tong,[1] David T. Sandwell,[1] Benjamin A. Brooks,[3] and Michael G. Bevis[4]

Received 3 May 2011; revised 8 August 2011; accepted 20 August 2011; published 3 November 2011.

[1] The great 27 February 2010 M_w 8.8 earthquake off the coast of southern Chile ruptured a ~600 km length of subduction zone. In this paper, we make two independent estimates of shear stress in the crust in the region of the Chile earthquake. First, we use a coseismic slip model constrained by geodetic observations from interferometric synthetic aperture radar (InSAR) and GPS to derive a spatially variable estimate of the change in static shear stress along the ruptured fault. Second, we use a static force balance model to constrain the crustal shear stress required to simultaneously support observed fore-arc topography and the stress orientation indicated by the earthquake focal mechanism. This includes the derivation of a semianalytic solution for the stress field exerted by surface and Moho topography loading the crust. We find that the deviatoric stress exerted by topography is minimized in the limit when the crust is considered an incompressible elastic solid, with a Poisson ratio of 0.5, and is independent of Young's modulus. This places a strict lower bound on the critical stress state maintained by the crust supporting plastically deformed accretionary wedge topography. We estimate the coseismic shear stress change from the Maule event ranged from −6 MPa (stress increase) to 17 MPa (stress drop), with a maximum depth-averaged crustal shear-stress drop of 4 MPa. We separately estimate that the plate-driving forces acting in the region, regardless of their exact mechanism, must contribute at least 27 MPa trench-perpendicular compression and 15 MPa trench-parallel compression. This corresponds to a depth-averaged shear stress of at least 7 MPa. The comparable magnitude of these two independent shear stress estimates is consistent with the interpretation that the section of the megathrust fault ruptured in the Maule earthquake is weak, with the seismic cycle relieving much of the total sustained shear stress in the crust.

Citation: Luttrell, K. M., X. Tong, D. T. Sandwell, B. A. Brooks, and M. G. Bevis (2011), Estimates of stress drop and crustal tectonic stress from the 27 February 2010 Maule, Chile, earthquake: Implications for fault strength, *J. Geophys. Res.*, *116*, B11401, doi:10.1029/2011JB008509.

1. Introduction

[2] On 27 February 2010, an earthquake of magnitude 8.8 struck off the coast of Maule, Chile, the sixth largest since recording began. This event represents the latest release of strain energy built up along the locked megathrust zone consisting of the oblique subduction of the Nazca plate beneath the South American plate at a rate of 65 mm/yr [*Kendrick et al.*, 2003]. Prior to this event, the last major rupture in the region occurred in 1835, such that the Maule region had been identified as a seismic gap [e.g., *Lorito et al.*, 2011; *Madariaga et al.*, 2010; *Moreno et al.*, 2010]. Following the earthquake, several groups worked to determine the coseismic slip distribution and moment release. Peak coseismic slip has generally been estimated in the range of 16–20 m, with an average slip of 5–6.5 m and a moment release of 1.8–2.6 × 10^{22} N m [*Delouis et al.*, 2010; *Lay et al.*, 2010; *Lorito et al.*, 2011; *Pollitz et al.*, 2011; *Tong et al.*, 2010b; *Vigny et al.*, 2011]. The slip is distributed in such a way that it at least partially filled in the identified seismic gap.

[3] The slip along this locked plate boundary is part of the broader setting of a downgoing oceanic slab contributing to the formation of topography, both through continental

[1]Scripps Institution of Oceanography, University of California, San Diego, California, USA.
[2]Now at Volcano Science Center, U.S. Geological Survey, Menlo Park, California, USA.
[3]School of Ocean and Earth Science and Technology, University of Hawai'i at Manoa, Honolulu, Hawaii, USA.
[4]School of Earth Sciences, Ohio State University, Columbus, Ohio, USA.

0148-0227/11/2011JB008509

orogenic processes such as crustal shortening and more localized coastal processes such as sediment accretion. The height of this topography can be used to constrain the strength of the subduction megathrust, measured by either the sustained shear stress or the coefficient of friction on the fault. *Lamb* [2006] estimated the mean shear stress required to support the elevation of the high Andes at ~37 and ~15 MPa in northern and southern Chile, respectively, consistent with estimates from previous thermal modeling studies in megathrust regions. This stress was principally transmitted through the lower crust, with smaller portions transmitted through the upper crust and mantle. *Seno* [2009] used a similar force balance method and estimated that mean shear stress along subduction zones is generally tens of megapascals, with the value in northern Chile on the higher end of that range, greater than 80 MPa. *Zhong and Gurnis* [1994] used a dynamic model of developing trench topography to estimate shear stress on subduction faults in the range of 15 to 30 MPa. More recently, *Tassara* [2010] determined that fore-arc topography is spatially correlated with various earthquake parameters and likely plays at least some part in controlling seismogenic behavior. Other studies have used observations of present-day topography to constrain the effective coefficient of friction on subduction thrusts to be less than 0.2 [*Cattin et al.*, 1997] or 0.03 to 0.09 [*Lamb*, 2006].

[4] The broad discussion about fault strength has stemmed from a few key kinds of observations. Low stress drops and the absence of a strong fault-related heat flow anomaly along the San Andreas fault in California suggest that the stress stored and released over the seismic cycle is much lower than the large in situ stresses that are both observed in borehole measurements and predicted from laboratory faulting experiments [e.g., *Byerlee*, 1978; *Scholz*, 2000; *Zoback*, 2000]. These observations may be reconciled if faults in general, or perhaps the San Andreas specifically, are weak with a coefficient of friction ~0.1. However, other lines of evidence, such as the angle between the principal stress axes and a particular fault trace, have led to inconsistent interpretations of fault friction [*Hardebeck and Michael*, 2004]. At subduction zones, observations of the reactivation of outer rise normal faults have shown that while these faults are weaker than newly formed faults, they still have a coefficient of friction of 0.6, in line with the predictions of laboratory experiments [*Billen et al.*, 2007]. Along the southern Chilean megathrust, low friction coefficients are suggested to relate to an abundance of accumulated sediment that acts as a trench lubricant [*Lamb and Davis*, 2003].

[5] In this paper, we provide two independent estimates of shear stress in the rupture area of the Maule event. In the first, we calculate the coseismic stress change on the rupture surface. The complete interferometric synthetic aperture radar (InSAR) coverage over the rupture area of the Maule event provided a unique opportunity to derive a detailed slip model needed to estimate the spatially variable stress change from the event. In addition, we present a new formulation to directly estimate the three-dimensional (3-D) crustal stress field on the megathrust fault exerted by local surface and Moho topography, constrained by gravity observations. We can then determine the minimum value of stress in the crust applied by tectonic forces required to both offset the stress exerted by topography and to maintain a stress field orientation consistent with that of the stress released in the earthquake. This idea is similar to previous studies that have estimated tectonic stress by balancing the loading of topography [e.g., *Lamb*, 2006], but it has the advantage of deriving its estimate from the short-wavelength topography immediately above the ruptured megathrust region. In this way, the estimate more directly assesses the stress in the crust at the seismogenic portion of the subduction zone, rather than relying on stress beneath the high Andes being transmitted several hundred kilometers back to the shallow megathrust region. By estimating both of these quantities independently, we have the opportunity, in this one instance, to make a direct comparison of the stress released in a major earthquake with a lower bound on the crustal-driving stress. In doing so, we are able to constrain the fraction of driving stress released in the seismic cycle versus that which is transmitted across the plate boundary, and we find evidence that the southern Chile subduction thrust is weak in the Maule area.

2. Minimum Stress Drop From the 27 February 2010 Maule Earthquake

[6] The coseismic displacement from the 2010 Maule, Chile, earthquake was observed in unprecedented detail using InSAR [*Tong et al.*, 2010b]. Several factors contribute to the quality of these observations. First, radar interferograms acquired with the L-band Advanced Land Observatory Satellite (ALOS) [*Shimada et al.*, 2010] have improved coherence relative to C-band radar. Second, recent processing advances allow interferograms to be made from radar images acquired in the scanning synthetic aperture radar (ScanSAR) mode [e.g., *Bamler and Eineder*, 1996; *Ortiz and Zebker*, 2007; *Sandwell et al.*, 2008; *Tong et al.*, 2010a, 2010b]. This is especially important because the descending passes made days after the Maule main shock were recorded in ScanSAR mode and recorded the deformation along the entire coastline in a single track. (These interferograms and sampled displacement data are available, along with the updated slip model and stress drop model presented in this paper, online at ftp://topex.ucsd.edu/pub/chile_eq/). A third factor contributing to the quality of these coseismic observations is that the region of interest is a subduction zone with a shallow dip. Spatial variations in coseismic slip on the fault are thus better represented by spatial variations in surface displacement compared with those in a vertical fault plane, even though the shallowest portions of the fault lie offshore, where displacement is unobservable by InSAR. The observations from interferometry need to be combined with observations of coseismic displacement from a network of GPS stations in the region, required for constraining the absolute offset.

[7] *Tong et al.* [2010b] inverted near-field geodetic data from InSAR line-of-sight (LOS) displacement and 13 continuous GPS stations to model coseismic slip on a single dipping plane 670 km long by 260 km wide, approximating the geometry of the shallow megathrust with a strike 16.8° EofN and a 15° dip to the east. The inversion assumes an isotropic homogeneous elastic half-space [*Fialko*, 2004;

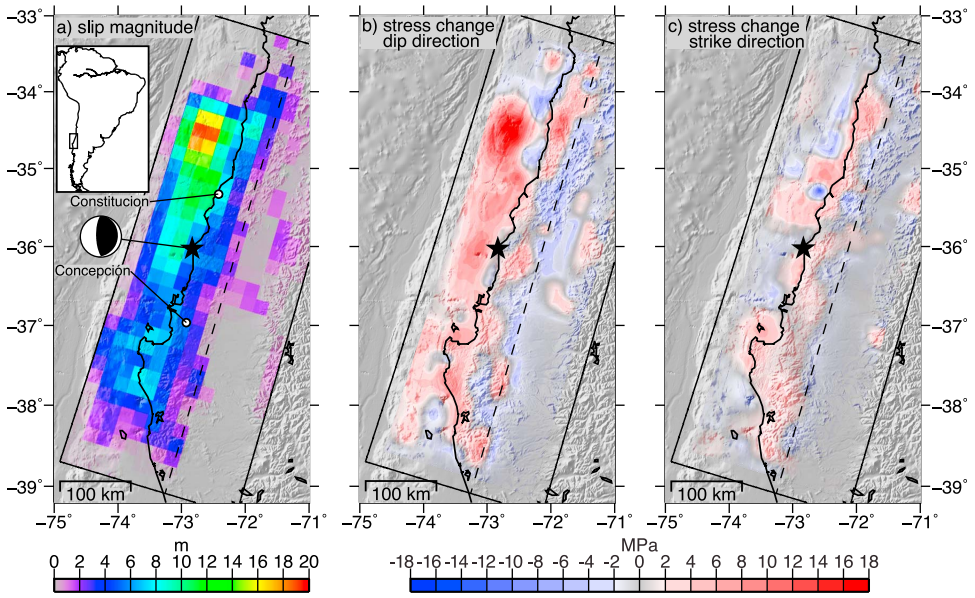

Figure 1. (a) Coseismic slip magnitude from joint inversion of GPS and InSAR data. Static shear stress change from Maule, Chile, earthquake derived from slip model shown in Figure 1a resolved in the (b) dip-slip and (c) strike-slip directions. The stress change is shown below 5 km depth, where the result from the FFT calculation method is most reliable. Positive (negative) shear stress values correspond to stress release (buildup). The focal mechanism from the Maule event is shown with a line to the main shock hypocenter, indicated by a black star. Solid and dashed lines denote the edge of the model and approximate Moho depth at 40 km, respectively.

Okada, 1985] and resolved slip on the dipping fault plane with a resolution of approximately 40 km × 40 km. Since the publication by *Tong et al.* [2010b], coseismic observations from an additional 9 continuous GPS stations in the rupture near field have become available [*Pollitz et al.*, 2011; *Vigny et al.*, 2011]. (For further information about the added sites, CONS, DGF1, MAUL, PORT, SJAV, VALN, VNEV, RCSD, and ROBL, see *Vigny et al.* [2011, Table S1]). These stations are located near the high-slip patch toward the northern end of the rupture zone and help constrain the extent and magnitude of the slip. The updated slip model is shown in Figure 1a and includes the full set of coseismic geodetic observations recorded from this earthquake.

[8] This refined model shares general features with the previous model: (1) the maximum slip is at ~20 km depth and the downdip rupture limit is about 40–45 km depth, (2) there is an area of relatively low slip (~7 m) offshore west of Concepción, and (3) there is a relatively high slip area (~10 m) at ~30 km depth northeast of the peak slip. Compared with that of the previous model, the major slip area ~140 km north of the epicenter increases slightly to ~20 m and becomes more localized. Although the changes to the slip model are slight, the additional GPS observations are more important for constraining the stress change from this earthquake.

[9] We compute the static shear-stress change from the refined coseismic slip model using a fast Fourier transform (FFT) method [*Andrews*, 1980; *Ripperger and Mai*, 2004], chosen because of its computational efficiency that allows the exploration of multiple model parameters. The 20 km × 20 km gridded slip model is initially downsampled via bicubic interpolation to a 1 km × 1 km grid, which serves as the input for the stress-change calculation. This downsampling ensures that the resulting stress features are stable and that no stress artifacts that are due to slip model resolution are introduced. Shear strain change is computed from the slip model and then converted to shear stress change using an average shear modulus of 40 GPa.

[10] Previously this method has been used successfully on vertical fault planes, employing a mirror-image technique to satisfy the free-surface zero-traction boundary condition for strike-slip-induced stress change. For inclined faults, however, it has the disadvantage of neglecting the free-surface boundary condition for dip-slip-induced stress change. We tested the efficacy of using the FFT method on a simple shallow dipping thrust fault by comparing the static-stress drop of the FFT method with that of an exact half-space formulation [*Okada*, 1992]. The effect of neglecting the half-space boundary condition was at most about 20% near the top edge of the fault (0–3 km depth), with the disagreement between the two solutions decreasing with depth. Below 5 km depth, the static-stress-change estimates from the FFT and half-space methods agree well, so the FFT method solution is considered reliable.

[11] The static shear stress change in the dip-slip direction derived from the full slip model is shown in Figure 1b for depths of 5 km and below. The static stress change varies approximately from 17 MPa (stress drop) to −6 MPa (stress increase) over the fault plane. The variation of the static stress drop follows the variation of the slip model, as expected, and a significant portion of the stress drop is contributed from thrust motion at the asperity 140 km north

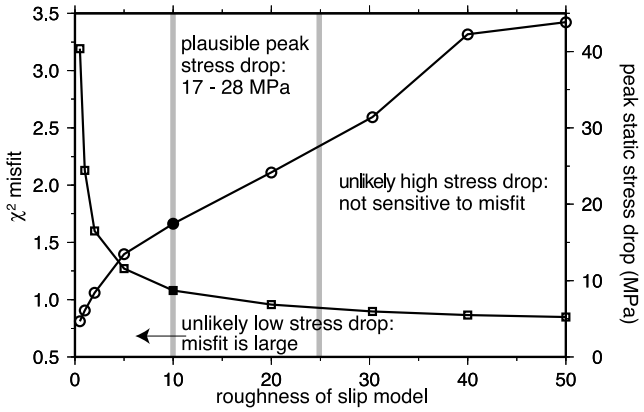

Figure 2. The χ^2 misfit of inverted slip model to geodetic observations (squares) and stress drop derived from slip model (circles) as a function of nondimensional roughness parameter (see supplementary material of *Tong et al.* [2010b]). The peak static-stress drop is calculated at 72.55°W, 34.53°S, within the main slip asperity north of the epicenter. The filled symbols indicate the roughness value of the stress change model shown in Figure 1. We interpret this as a lower bound of peak stress drop estimated from geodetic inversion.

of the epicenter. Stress change resolved in the strike-slip direction (Figure 1c) is between −5 MPa (stress increase) and 5 MPa (stress drop), and it may be safely neglected since the coseismic slip and stress change was dominated by thrust motion.

[12] The calculation of stress change from a given slip model is straightforward and depends on only a choice of shear modulus for relating shear strain to shear stress. The peak shear stress value is a direct consequence of the peak slip model curvature (i.e., the second derivative of slip on the fault plane), which can be characterized by a nondimensional roughness parameter describing the weight given to a smoothing requirement in the slip inversion (see supplementary material to *Tong et al.* [2010b]). Figure 2 demonstrates the dependence of both slip model misfit and peak static stress drop on the nondimensional roughness parameter. The χ^2 misfit reduces from 3.2 to 1.1 as roughness increases from 1 to 10, clearly illustrating that the additional roughness is required to explain the geodetic observations. However, increasing slip model roughness from 10 to 25 provides only a marginally improved misfit of 0.95. For roughness greater than 25, the decrease in misfit is negligible, indicating that the geodetic observations cannot justify the fine-scale features of a model this rough, though, strictly speaking, neither can they rule them out.

[13] The peak stress drop is heavily dependent on model roughness, so it is important to identify the range of acceptable slip models that provide a reasonable fit to the geodetic observations. A model roughness of 10–25 corresponds to a range of likely stress drops of 17–28 MPa, and the slip and stress change models shown in Figure 1 are calculated with a roughness of 10, corresponding to a 17 MPa stress drop. Again, this is strictly a lower bound on the possible peak stress drop, but a higher stress drop would require a slip model that is more rough than can be justified by the data. When the preferred stress change is averaged throughout the crust (top 40 km, or 154 km along dip), the mean stress drop is ~4 MPa.

3. Minimum Tectonic Stress Estimate From Topography

[14] In addition to the shear stress released in a major earthquake, we can also estimate the stress applied to the crust from plate-driving forces by calculating the minimum crustal stress field that could simultaneously support the local topography and maintain an orientation consistent with a subduction thrust plate boundary. Topography formation is subject to many different processes, but in the region of the Maule earthquake the topography may be divided by wavelength into two portions. The long-wavelength topography across the coast of South America (i.e., wavelengths greater than 2π times the depth of compensation) is dominated by the rise from the offshore subduction trench to the high Andes and is supported by a combination of isostatic compensation and dynamic buoyancy that is due to convecting upper mantle material. The short-wavelength topography (i.e., wavelengths less than ~350 km) in the megathrust region is dominated by an accretionary wedge of material scraped from the subducting slab. This wedge is built through processes of plastic deformation such that the state of stress supporting this topography is maintained at the level of critical failure [*Dahlen*, 1990]. The height of this critical wedge topography is limited by the portion of the lithosphere that can sustain shear stress (i.e., the depth to the brittle-ductile transition).

[15] It was previously observed that the coseismic slip of the Maule earthquake was negligible below the fore-arc Moho, such that no shear stress was relieved in the continental mantle from this event (Figure 1). We therefore infer that the stress state of critical plastic failure related to the accretionary wedge topography in this region is sustained throughout the crust, but not below the Moho. This suggests that the in situ crustal stress state in this region can be directly related to the height of the local short-wavelength topography. Furthermore, if the processes by which the local topography formed behaved as roughly elastic-perfectly-plastic, then the critical stress state maintained throughout the crust can be estimated as that which the critical topography would exert in an elastic plate. The model of an elastic plate loaded by local surface and Moho topography may thus be used to estimate the in situ deviatoric nonlithostatic stress state throughout the crust in a region where topography height is critically limited by the strength of the crust.

[16] We can calculate the 3-D stress exerted by the load of this short-wavelength topography and the corresponding buoyant load from the Moho at the surfaces of a uniformly thick elastic plate (Figure 3). We do this with a semianalytic model in which an analytic solution for the stress within a thick elastic plate loaded on the surface and base by nonidentical point loads (derived in Appendix A) is numerically convolved with the actual observed shape of the surface and Moho topography in the Fourier domain. We can then examine the 3-D stress field along a dipping plane representing the locked seismic zone, where we expect the strength of the plate boundary region to be limited in order to constrain the magnitude of the applied driving stresses.

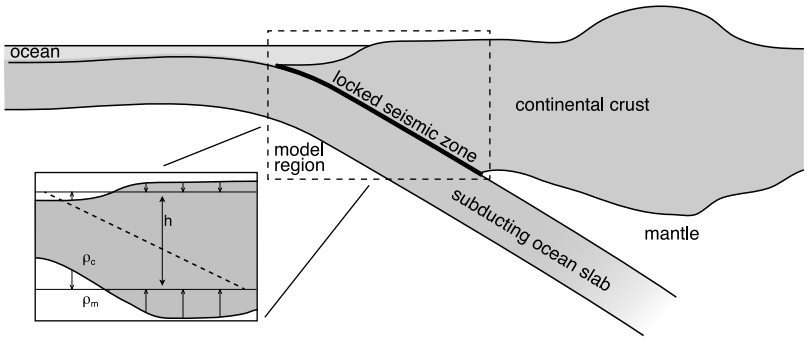

Figure 3. Schematic illustration of megathrust geometry showing the locked seismogenic zone between the subducting slab and the continental crust. The model region, indicated by the dashed box, is represented mathematically as a uniform thick plate loaded by surface and Moho topography, as shown in the inset. The dashed line indicates the dipping fault plane, representing the locked seismic zone, on which the calculated stress field is resolved.

[17] In order to calculate the stress state exerted by topography, the surface topography and bathymetry [*Becker et al.*, 2009] is first high-pass filtered using a cosine taper between spherical harmonics 100 and 140 (corresponding to wavelengths between 300 and 400 km). The shape of the Moho is related to the surface topography by flexure, constrained by observations of the gravity anomaly in the region that have also been high-pass filtered (continent region from *Pavlis et al.* [2008]; ocean region from *Sandwell and Smith* [2009]). For a 40 km thick crust, consistent with the estimates from receiver functions [*Lloyd et al.*, 2010; *Sick et al.*, 2006; *Yuan et al.*, 2002], the ~250 mGal anomaly across the region is fit to an RMS of 31 mGal with an effective elastic thickness of 3 km and a density of 2600 kg/m^3.

[18] Stress values calculated in an elastic plate will necessarily depend somewhat on the elastic moduli. We assume a Young's modulus of 70 GPa, but that the Poisson ratio of the material may vary. Strictly speaking, we want to find the stress state with the smallest critical stress in order to identify the strict minimum possible tectonic stress magnitude. The critical stress in the crust is measured by calculating the second invariant of the deviatoric stress tensor, i.e., the von Mises stress. We show in Appendix A that the smallest deviatoric stress the wedge topography could exert in the crust corresponds to a Poisson ratio of $\nu = 0.5$, or that of a load acting on an incompressible elastic solid. We use this parameter in order to ensure the calculation gives a strict lower bound on the size of the deviatoric stress sustained by the deformed crust. In practicality, however, this stress differs very little from that in an elastic solid with $\nu = 0.25$ when topography is nearly Airy compensated, as it is in this region.

[19] Appendix A also shows that, because we use stress to calculate stress, with strain involved only as an intermediate step, the thick plate stress solution is actually independent of Young's modulus. For the calculations presented here, Young's modulus is only a factor in the flexural rigidity used to determine the shape of the Moho from gravity analysis. As such, the results are robust to the choice of a single representative value of Young's modulus, rather than accounting for depth variations of Young's modulus throughout the crust.

[20] The stress required to support topography is calculated along the locked interface between the subducting slab and the overriding crust, using the same fault geometry as that of the coseismic stress change model in the previous section. We first resolve this 3-D stress into reverse-slip shear stress on the megathrust fault plane (Figure 4a), where positive (negative) values indicate that a reverse (normal) dip slip is favored. Across most of the fault plane, the load of the topography by itself induces a normal stress state, except in the very low regions of the offshore trench and onshore sediment basin. The largest negative shear-stress values are ~7 MPa, indicating that the tectonic driving forces in this region must contribute at least this much shear stress in order to overcome the influence of topography and ensure a thrust absolute stress state.

[21] We can further constrain the magnitude of the plate-driving stress acting on the fault plane by comparing the 3-D orientation of the stress derived from topography with that of the centroid moment tensor solution of the Maule event (National Earthquake Information Center (NEIC)). The total in situ stress orientation across the ruptured region should be largely consistent with the focal mechanism orientation. We can quantitatively assess differences in stress orientation by defining a goodness-of-fit parameter $\xi \in [0,1]$, such that

$$\xi = \begin{cases} 0 & \text{if model and event stress regimes differ} \\ \left(\vec{v}_1^{\,model} \cdot \vec{v}_1^{\,event} + \vec{v}_2^{\,model} \cdot \vec{v}_2^{\,event} + \vec{v}_3^{\,model} \cdot \vec{v}_3^{\,event}\right)/3 & \text{else} \end{cases}, \tag{1}$$

where $\vec{v}_i^{\,model}$ and $\vec{v}_i^{\,event}$ are the eigenvectors (principal stress axes) of the 3-D stress tensor of the model and the event, respectively. The definition of stress regime involves the plunge angle of each principal stress axis, following the convention of the World Stress Map catalog [e.g., *Zoback*, 1992]. The mean of this parameter over each location on the fault plane $\bar{\xi}$ tests the fit of each modeled stress field.

[22] Figure 4b shows the value of ξ along the rupture region for the stress field calculated from topography alone. The lower-hemisphere projection "beach balls" indicate the orientation of the modeled topography stress field, with the tension principal stress axis oriented through the shaded quadrants and the pressure axis oriented through the unshaded quadrants. These are compared with the Maule event focal mechanism, shown by the larger beach ball on the side. As expected, the stress from topography alone is

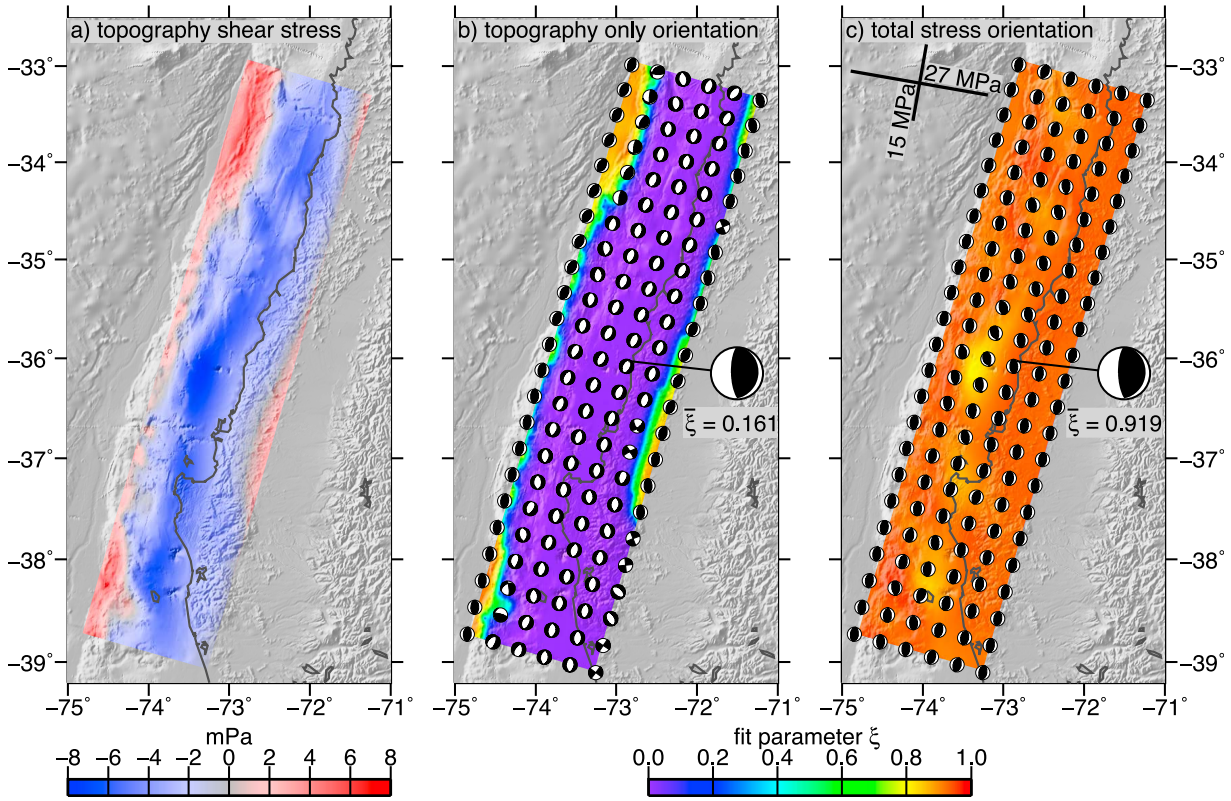

Figure 4. (a) Magnitude of crustal stress field exerted by surface and Moho topography, indicated as the dip-slip shear stress resolved onto the dipping fault plane. Positive (negative) shear stress values indicate that reverse (normal) dip-slip motion is preferred. (b) Orientation of crustal stress field exerted by surface and Moho topography (beach balls) and parameter ξ (shading), indicating the fit between model stress field orientation and that indicated by the Maule event focal mechanism. (c) Fit parameter ξ (shading) and orientation (beach balls) of smallest stress field capable of both supporting short-wavelength topography and maintaining a stress orientation consistent with that of the Maule event throughout rupture region. Stress field includes an additional 27 MPa compression at 100°EofN and 15 MPa compression at 10°EofN.

not consistent with the orientation of the Maule event across most of the fault plane. Only the offshore trench region is in a properly oriented thrust regime, while the onshore coastal foothills are in a normal or strike-slip regime. This poor fit is quantitatively indicated by the low mean fit value of $\bar{\xi} = 0.161$.

[23] To reconcile this stress mismatch, we add a regionally uniform horizontal stress field (representing the depth-averaged tectonic plate-driving stress in the crust), consisting of three free parameters (two principal horizontal stress magnitudes and the orientation angle of the axes), to the topography-supporting stress field. We search this parameter space and define the conditions that maximize $\bar{\xi}$, the fit between the model stress field and the Maule event. The best orientation of the added stress is nearly trench-parallel and trench-perpendicular, favoring a slightly counterclockwise orientation.

[24] Contours of $\bar{\xi}$ with respect to applied trench-perpendicular and trench-parallel stresses (Figure 5) reveal two requirements on the added stress magnitude in order to ensure that the combined stress field is aligned with that of the earthquake. First, there must be a trench-parallel compression of at least 15 MPa above lithostatic pressure. Second, trench-perpendicular compression must exceed trench-parallel compression by at least 12 MPa for a total of at least 27 MPa of trench-perpendicular compression. Any added stress that satisfies both of these conditions will result in a properly oriented thrust-regime stress field along the entire megathrust fault plane. The estimate of stress from topography thus provides a firm lower bound on the magnitude of nonlithostatic stress acting in the region of the Maule earthquake. Figure 4c shows the value of ξ along the ruptured fault plane for the topography stress field plus the smallest satisfactory representation of additional tectonic stress (15 MPa compression at 10°EofN and 27 MPa compression at 100°EofN). With this addition, the mean fit of the stress field orientation improves to $\bar{\xi} = 0.919$, indicating that across most of the fault plane the model stress field is consistent with the orientation of the Maule event.

[25] A trench-perpendicular compression of 27 MPa resolved onto a 15° dipping plane corresponds to 7 MPa of resolved reverse-slip shear stress. This value is expected, as it balances the minimum value of the topography-only shear stress observed in Figure 4a, ensuring that the total stress field favors reverse dip slip over normal dip slip. However, ensuring a thrust regime throughout the fault plane also

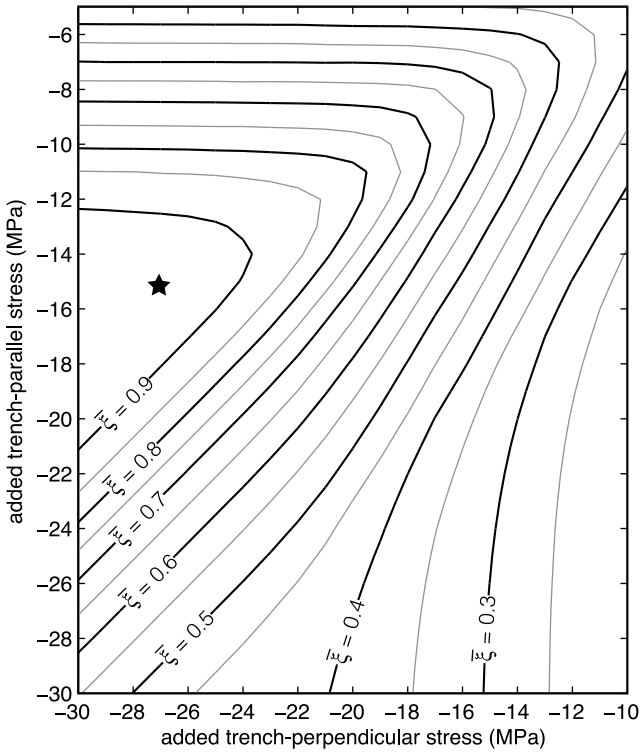

Figure 5. Contours of mean fit parameter $\bar{\xi}$ averaged over the entire fault plane as a function of roughly trench-perpendicular (100°EofN) and trench-parallel (10°EofN) additional tectonic driving stress.

requires trench-parallel compression to exceed vertical compression. Otherwise the stress could favor reverse slip over normal slip but still be in a dominantly oblique or strike-slip regime. The requirement for at least 15 MPa of trench-parallel compression corresponds physically to the difference between the vertical and trench-parallel stresses exerted by topography alone. Adding trench-parallel stress ensures that the least-compressive stress is vertical. It seems, therefore, that in order to maintain a properly oriented stress field, the regional driving tectonic stress must maintain at least 12 MPa deviatoric stress.

4. Discussion

[26] The stress drop of a single earthquake can vary widely, from ~10^{-1} to 10^2 MPa [e.g., *Allmann and Shearer*, 2009; *Hardebeck and Aron*, 2009]. The peak value of our slip-model-derived estimate at 17 MPa is on the higher end of this range, well above the 3–4 MPa median stress drop estimated from the corner frequency of the seismic spectra for a global catalog of events. However, the depth-averaged stress drop estimate of 4 MPa may be a better quantity to compare with seismic estimates of stress drop. While the peak stress drop depends on the roughness parameter chosen when inverting the slip model (Figure 2), the depth-averaged stress drop is largely independent of model roughness. This depth-averaged estimate is consistent with previous observations that intraplate earthquakes deep in the subducted slab in Chile have a higher stress drop, around 9 MPa, while interplate earthquakes along the contact megathrust zone between the plates have a lower stress drop, around 3 MPa [*Leyton et al.*, 2009].

[27] Previous studies have disagreed over whether there is any correlation between event stress drop and event magnitude, depth, or regime. Larger stress drops have been associated with thrust events along the San Andreas fault in California [*Hardebeck and Aron*, 2009], but a global study of stress drops found rather that the stress drop is larger for strike-slip events than for thrust events, though it could be that some of the assumptions of a seismic estimation of stress drop (e.g., a circular slip patch, constant rupture velocity) break down for very large earthquakes [*Allmann and Shearer*, 2009]. The *M* 8.8 Maule earthquake is, to date, the sixth largest earthquake since modern recording began, and yet has a stress-drop magnitude equal to the global average. This corroborates the previous observations that event magnitude and stress drop are not correlated.

[28] One thing we may be able to infer from a spatially distributed model of stress drop is which regions of fault slip, if any, may have been loaded with increased shear stress by the rupture. Our model suggests the largest area of shear stress increase (~—5 MPa) was downdip in the lowest crust north of the main shock hypocenter but south of the main slip asperity. Further updip and offshore, we observe widespread dominant stress release. This is in contrast to observations of Coulomb stress change observed by *Lorito et al.* [2011], who found a stress increase of up to 3 MPa broadly in the shallowest portions of the rupture area and specifically closer to the coastline between 36°S and 37°S. In that zone we observe a small asperity-adjacent patch on which shear stress may have increased by ~1 MPa, but we see no evidence that a broader stress increase occurred.

[29] While our estimate of depth-averaged cosesmic stress drop is robust, our tectonic mean crustal shear stress estimate is a minimum for two reasons. First, the assumption of material incompressibility calculates the stress state with the smallest possible deviatoric stress that the topography as a load could exert, such that our calculation of the short-wavelength stress is a minimum. Such an assumption may be appropriate when considering the support of short-wavelength topography. *Dahlen* [1981] proposed that the deviatoric stress in unflexed regions of oceanic lithosphere is the minimum state required to support topography and found that this corresponded to the case of an incompressible material, though this was not explicitly stated. Also, for nearly Airy compensated topography, the deviatoric stress magnitude differs by less than 10% between an incompressible material with $\nu = 0.5$ and an elastic material with $\nu = 0.25$. Thus, we are confident that our calculation closely estimates the spatial variations in the magnitude of stress sustained throughout the crust at this wavelength.

[30] The second reason our mean crustal shear stress estimate is a minimum is because we have made no assumptions about the forces responsible for ongoing processes beyond the locked seismic zone. Any stress responsible for net plate motion that is sustained through the crust must be in addition to the minimum long-wavelength stress we have identified as necessary to support the observed topography and stress regime. It is interesting that our minimum estimate of crustal shear stress is about half that of previous estimates of tectonic shear stress throughout the entire plate that focused on the balance of long-wavelength topography with tectonic stress

[*Lamb*, 2006; *Seno*, 2009; *Zhong and Gurnis*, 1994]. While this could simply indicate that the in situ crustal stress is actually larger than that estimated in this paper, it may instead indicate that while the bulk of plate strength resides in the continental crust [e.g., *Jackson et al.*, 2008], some lithospheric strength is maintained in the continental mantle, despite its aseismicity.

[31] The comparison of our crustal tectonic stress estimate with our stress drop estimate from the Maule event has some implications for our understanding of fault strength in the region. If the coseismic stress drop exactly equaled the crustal-driving stress, that would indicate that all of the stress was taken up in the seismic cycle and the downgoing motion of the slab, leaving no excess stress to be accommodated in back-arc mountain-building processes. This would correspond to a completely weak subduction fault, unable to sustain any amount of shear stress in the long term. In contrast, if the coseismic stress drop was much less than the crustal-driving stress, a large quantity of stress would be available to be accommodated in continent-deformation processes. This would indicate a very strong subduction fault, transmitting most of its sustained stress across the plate boundary. In actuality, our estimate of crustal-driving stress is moderately larger than the coseismic stress drop. The depth-averaged shear stress drop at the northern asperity is 4 MPa, compared with at least 7 MPa resolved tectonic shear stress required to support topography.

[32] If these numbers accurately represent the stresses sustained by the fault and relieved through the seismic cycle, then our estimates indicate a fairly weak crustal fault in which major earthquakes relieve much of the total stress. This would be consistent with modeling studies that indicate a low effective coefficient of friction (less than 0.2) is required on subduction thrust faults in order to be consistent with observations of arc front topography [*Cattin et al.*, 1997; *Lamb*, 2006]. Because the crustal-driving stress estimate is strictly a minimum, the analysis presented here cannot absolutely determine that the southern Chilean subduction thrust is weak. However, the only way it could be strong is if either the tectonic stress magnitude in the crust is much larger than the minimum stress required to sustain the observed topography and stress regime, meaning a substantial portion of plate driving stress is transmitted through the crust, or if the stress drop from this event was anomalously low for this region. Large crustal stress transmission seems particularly unlikely, however, because at this latitude there has been little crustal shortening in the back arc [*Brooks et al.*, 2003]. In addition, the calculated coseismic stress drop does not seem anomalously low compared with global averages, though there are few observations of stress drop in this exact region to compare. We therefore prefer an explanation that the section of fault ruptured in the Maule event is fairly weak.

5. Conclusions

[33] In this paper, we have made two independent estimates of shear stress in the crust in the region of the M_w 8.8 Maule, Chile, earthquake. In the first, we have combined observations from InSAR and GPS to develop a coseismic slip model for the event and used this model to calculate the spatially variable static shear stress change along the fault from the rupture. We estimate the stress change from this event varied between −6 MPa (stress increase) to 17 MPa (stress drop). When averaged through the crust, this corresponds to a maximum shear-stress drop of 4 MPa.

[34] In the second, we have calculated the stress field exerted by surface and Moho topography loading the crust and have related that to the critical stress level sustained in the support of the accretionary wedge topography in the rupture region. We observe that long-wavelength plate-driving forces, regardless of their exact mechanism, must contribute at least enough stress in the crust to both support the observed topography variations and ensure that the 3-D orientation of the stress field is consistent with the in situ stress field indicated by the focal mechanism of the Maule event. We can therefore identify the following constraints on the tectonically applied stress in the crust at this location: Trench-parallel compression must be at least 15 MPa, and trench-perpendicular compression must exceed trench-parallel compression by at least 12 MPa for a total of at least 27 MPa of trench-perpendicular compression. When resolved into dip-slip shear stress on the subduction fault plane, this corresponds to a mean crustal shear stress of at least 7 MPa.

[35] The comparable magnitudes of these two independent estimates suggest that the seismic cycle relieves a quantity of stress similar to that required to sustain the observed topography and stress orientation, consistent with a weak megathrust fault that transmits very little compression to the back arc. These observations are consistent with previous studies that estimate a low coefficient of friction for subduction faults as well as a low mean shear stress along the subduction interface of southern Chile in particular. Detailed geodetic imaging of the coseismic slip from the Maule event as well as the development of a force balance model derived specifically to constrain the magnitude of crustal tectonic stress has allowed us to investigate the stress state in a narrow geographic region. We are thus able to place strict lower bounds on the absolute magnitude of the deviatoric stress in the lithosphere at this location.

Appendix A: Derivation of Loaded Thick Elastic Plate Green's Function

A1. Method and Boundary Conditions

[36] This appendix contains the derivation of the 3-D stress field generated by top and bottom loading of an elastic plate of thickness h. Solutions to the Boussinesq problem for balancing vertical tractions on a surface were originally developed for an elastic half-space [*Boussinesq*, 1885; *Steketee*, 1958]. More recently, similar methods have been followed to derive solutions for balancing vertical tractions on the surface of an elastic plate overlying a viscoelastic half-space [*Luttrell and Sandwell*, 2010; *Luttrell et al.*, 2007; *Smith and Sandwell*, 2004]. Here we again follow the approach of *Steketee* [1958] to solve a Boussinesq-like problem in which we apply two distinct loads to the surfaces of an elastic plate.

[37] The model is semianalytic in that the Green's function stress from nonidentical vertical point loads at the top and bottom of the plate is analytically derived below and then numerically convolved with the actual two-dimensional (2-D) shape of the load to get the 3-D stress field. This

method of calculation is advantageous because it is numerically efficient, though it does require that the vertical structure of the model earth be simple. The loads at the top and bottom of the plate ($f(x, y)$ at $z = 0$ and $g(x, y)$ at depth $z = h$, respectively) may be arbitrarily intricate and need not be related, though Moho shape is generally related to surface topography through flexure. The only restrictions on the loads come from the FFT convolution, which requires that the zero-wave-number component of the force be zero and that the computational region be wider than the longest wavelength we are interested in. The compensation of very long wavelength loads can be adequately described by thin-plate flexure, while the compensation of short-wavelength loads can be described by an elastic half-space. We are primarily interested in the intermediate-wavelength loads between these domains.

[38] The response of a plate to a vertical point load is radially symmetric; therefore only four boundary conditions are needed to describe the system. Shear tractions must vanish at the surfaces, and vertical normal tractions are defined by the applied loads. We treat the distributed loads as horizontally varying but applied at a single depth:

$$\sigma_{xz}(\vec{x}, 0) = 0, \tag{A1a}$$

$$\sigma_{xz}(\vec{x}, h) = 0, \tag{A1b}$$

$$\sigma_{zz}(\vec{x}, 0) = -f(\vec{x}), \tag{A1c}$$

$$\sigma_{zz}(\vec{x}, h) = -g(\vec{x}). \tag{A1d}$$

Stress is positive in extension and negative in compression, and z is positive up. If $f(\vec{x})$ and $g(\vec{x})$ are positive numbers, both applied normal stresses are compressive (negative). Note that despite the inherent radial symmetry of the problem, we continue the derivation in Cartesian coordinates for simplicity, and note here that the additional boundary conditions, requiring that the other vertical shear stresses σ_{yz} also vanish, are appropriate but redundant. Numerical FFTs are done in Cartesian coordinates on a global 1-min Mercator-projected grid divided into strips of latitude, and individual strips are merged using a cosine taper to reduce any effect from latitude seams.

A2. Stress in a Thick Elastic Plate

[39] As *Luttrell and Sandwell* [2010] did, we let displacement and stress be a function of the Galerkin vector potential Γ_i:

$$u_i = \Gamma_{i,kk} - \alpha\Gamma_{k,ki}, \tag{A2}$$

$$\sigma_{ij} = \lambda(1-\alpha)\delta_{ij}\Gamma_{l,kkl} + \mu\left(\Gamma_{i,kkj} + \Gamma_{j,kki}\right) - 2\mu\alpha\Gamma_{k,kij}, \tag{A3}$$

where α is a constant yet to be determined and stress above the lithostatic state σ_{ij} has been related to strain and displacement u_i through an elastic constitutive equation with Lamé parameters λ and μ. Note that we use the standard summation notation, such that a variable with a single subscript is a vector, a variable with two subscripts is a tensor, a repeated index indicates summation over the coordinates, and an index following a comma indicates differentiation with respect to that coordinate. Because the applied point loads are purely normal and applied on a horizontal free surface, we need retain only the third component of the Galerkin vector, such that $\Gamma_x = \Gamma_y = 0$ and $\Gamma_z = \Gamma$, which we call the Galerkin potential.

[40] When the equilibrium equations for a body in the absence of internal body forces or acceleration $\sigma_{ij,j} = 0$ are written in terms of the Galerkin potential, we find that by letting $\alpha = (\lambda + \mu)/(\lambda + 2\mu)$, the Galerkin potential must satisfy the biharmonic equation $\nabla^4\Gamma = 0$. After taking the 2-D horizontal Fourier transform of this equation, the solution form is recognized as

$$\Gamma\left(\vec{k}, z\right) = (A + B\beta z)e^{\beta z} + (C + D\beta z)e^{-\beta z}, \tag{A4}$$

where $\beta = 2\pi|\vec{k}| = 2\pi\sqrt{k_x^2 + k_y^2}$ is the horizontal wave number and (A, B, C, D) are coefficients to be determined by the boundary conditions (equations (A1a)–(A1d)).

[41] We may now express the components of the stress tensor (equation (A3)) in terms of Young's modulus E, Poisson ratio ν, horizontal wave number, and the Galerkin potential coefficients. The stress components relevant to the boundary conditions (equations (A1a)–(A1d)) are

$$\sigma_{xz}\left(\vec{k}, z\right) = -i\pi k_x \frac{E\beta^2}{1-\nu^2}\left[\begin{array}{l}(A + B(2\nu + \beta z))e^{\beta z} + \\ (C + D(-2\nu + \beta z))e^{-\beta z}\end{array}\right], \tag{A5a}$$

$$\sigma_{zz}\left(\vec{k}, z\right) = \frac{E\beta^3}{2(1-\nu^2)}\left[\begin{array}{l}(-A + B(1 - 2\nu - \beta z))e^{\beta z} + \\ (C + D(1 - 2\nu + \beta z))e^{-\beta z}\end{array}\right]. \tag{A5b}$$

This system of four equations and four unknowns can now be solved using a computer algebra system (Mathematica). The coefficients of the Galerkin potential are found to be

$$\Phi = \frac{\nu^2 - 1}{E\beta^3(1 + 2\beta^2h^2 - \cosh 2\beta h)}, \tag{A6a}$$

$$A = \Phi\left[\begin{array}{l}f\left(\vec{k}\right)[-2\nu(2\beta h + \sinh 2\beta h) + (-2\nu(1 - \cosh 2\beta h) - 2\beta^2h^2)] + \\ g\left(\vec{k}\right)[4\nu(\beta h\cosh\beta h + \sinh\beta h) + 2(1 - 2\nu)\beta h\sinh\beta h]\end{array}\right], \tag{A6b}$$

$$B = \Phi\left[\begin{array}{l}f\left(\vec{k}\right)[(1 - \cosh 2\beta h) + (2\beta h + \sinh 2\beta h)] + \\ g\left(\vec{k}\right)[2\beta h\sinh\beta h - 2(\beta h\cosh\beta h + \sinh\beta h)]\end{array}\right], \tag{A6c}$$

$$C = \Phi\left[\begin{array}{l}f\left(\vec{k}\right)[-2\nu(2\beta h + \sinh 2\beta h) - (-2\nu(1 - \cosh 2\beta h) - 2\beta^2h^2)] + \\ g\left(\vec{k}\right)[4\nu(\beta h\cosh\beta h + \sinh\beta h) - 2(1 - 2\nu)\beta h\sinh\beta h]\end{array}\right], \tag{A6d}$$

$$D = \Phi\left[\begin{array}{l}f\left(\vec{k}\right)[(1 - \cosh 2\beta h) - (2\beta h + \sinh 2\beta h)] + \\ g\left(\vec{k}\right)[2\beta h\sinh\beta h + 2(\beta h\cosh\beta h + \sinh\beta h)]\end{array}\right]. \tag{A6e}$$

When substituted back into equations (A4) and (A3), the six components of the stress tensor can be written as

$$\sigma_{xx}\left(\vec{k},z\right) = f\left(\vec{k}\right)\left[\frac{k_x^2}{\left|\vec{k}\right|^2}\left(C_f - S_f\right) - 2\nu S_f\frac{k_y^2}{\left|\vec{k}\right|^2}\right] + g\left(\vec{k}\right)\left[\frac{k_x^2}{\left|\vec{k}\right|^2}\left(C_g - S_g\right) - 2\nu S_g\frac{k_y^2}{\left|\vec{k}\right|^2}\right] \quad \text{(A7a)}$$

$$\sigma_{yy}\left(\vec{k},z\right) = f\left(\vec{k}\right)\left[\frac{k_y^2}{\left|\vec{k}\right|^2}\left(C_f - S_f\right) - 2\nu S_f\frac{k_x^2}{\left|\vec{k}\right|^2}\right] + g\left(\vec{k}\right)\left[\frac{k_y^2}{\left|\vec{k}\right|^2}\left(C_g - S_g\right) - 2\nu S_g\frac{k_x^2}{\left|\vec{k}\right|^2}\right] \quad \text{(A7b)}$$

$$\sigma_{zz}\left(\vec{k},z\right) = f\left(\vec{k}\right)\left[-C_f - S_f\right] + g\left(\vec{k}\right)\left[-C_g - S_g\right], \quad \text{(A7c)}$$

$$\sigma_{xy}\left(\vec{k},z\right) = \frac{k_x k_y}{\left|\vec{k}\right|^2}\left\{f\left(\vec{k}\right)\left[C_f - S_f + 2\nu S_f\right] + g\left(\vec{k}\right)\left[C_g - S_g + 2\nu S_g\right]\right\}, \quad \text{(A7d)}$$

$$\sigma_{xz}\left(\vec{k},z\right) = \frac{ik_x}{\left|\vec{k}\right|}\left[f\left(\vec{k}\right)S'_f + g\left(\vec{k}\right)S'_g\right], \quad \text{(A7e)}$$

$$\sigma_{yz}\left(\vec{k},z\right) = \frac{ik_y}{\left|\vec{k}\right|}\left[f\left(\vec{k}\right)S'_f + g\left(\vec{k}\right)S'_g\right], \quad \text{(A7f)}$$

with depth dependence for the normal stress components and the horizontal shear stress component given by the transfer functions

$$C_f = \frac{2\beta^2 h\zeta\cosh\beta z - \beta z\sinh\beta z - \beta z\sinh\beta(h+\zeta)}{1 + 2\beta^2h^2 - \cosh 2\beta h}, \quad \text{(A8a)}$$

$$C_g = \frac{2\beta^2 hz\cosh\beta\zeta - \beta\zeta\sinh\beta\zeta - \beta\zeta\sinh\beta(h+z)}{1 + 2\beta^2h^2 - \cosh 2\beta h}, \quad \text{(A8b)}$$

$$S_f = \frac{2\beta h\sinh\beta z + \cosh\beta z - \cosh\beta(h+\zeta)}{1 + 2\beta^2h^2 - \cosh 2\beta h}, \quad \text{(A8c)}$$

$$S_g = \frac{2\beta h\sinh\beta\zeta + \cosh\beta\zeta - \cosh\beta(h+z)}{1 + 2\beta^2h^2 - \cosh 2\beta h}, \quad \text{(A8d)}$$

where z is the depth from the top of the plate and $\zeta = h - z$ is the distance from the bottom of the plate. The transfer functions related to the bottom load $g(\vec{k})$ are depth-inverted versions of those related to the top load $f(\vec{k})$, such that any occurrence of z and ζ are interchanged. The transfer functions for the vertical shear stress components are related to those in equations (A8a)–(A8d) by derivatives with respect to depth, such that

$$S'_{(f,g)} = -\frac{1}{\beta}\frac{d}{dz}\left[C_{(f,g)} + S_{(f,g)}\right]. \quad \text{(A9)}$$

A3. Benchmarks of Limit Cases

[42] We numerically compared the stress solutions above with those of *Love* [1929] for a point load in an elastic half-space and confirmed that stress calculations match to within a factor of 10^{-3}. We also show that in the long-wavelength limit, these solutions reduce to the 2-D stress solutions for a thin elastic plate in which topography is exactly Airy compensated, such that $g(x, y) = f(x, y)$. We can simplify the full 3-D solution for the Airy-compensation case where $g(x, y) = f(x, y)$, such that the stress solution given in equations (A7a)–(A7f) to (A9) reduces to

$$\sigma_{xx} = f\left(\vec{k}\right)\left[\frac{k_x^2}{\left|\vec{k}\right|^2}[C - S] - 2\nu S\frac{k_y^2}{\left|\vec{k}\right|^2}\right], \quad \text{(A10a)}$$

$$\sigma_{yy} = f\left(\vec{k}\right)\left[\frac{k_y^2}{\left|\vec{k}\right|^2}[C - S] - 2\nu S\frac{k_x^2}{\left|\vec{k}\right|^2}\right], \quad \text{(A10b)}$$

$$\sigma_{zz} = f\left(\vec{k}\right)[-C - S], \quad \text{(A10c)}$$

$$\sigma_{xy} = f\left(\vec{k}\right)\frac{k_x k_y}{\left|\vec{k}\right|^2}[C - S + 2\nu S], \quad \text{(A10d)}$$

$$\sigma_{xz} = i\frac{k_x}{\left|\vec{k}\right|}f\left(\vec{k}\right)S', \quad \text{(A10e)}$$

$$\sigma_{yz} = i\frac{k_y}{\left|\vec{k}\right|}f\left(\vec{k}\right)S', \quad \text{(A10f)}$$

with transfer functions given by

$$C = \frac{\beta\zeta\cosh\beta z + \beta z\cosh\beta\zeta}{\sinh\beta h + \beta h}, \quad \text{(A11a)}$$

$$S = \frac{\sinh\beta z + \sinh\beta\zeta}{\sinh\beta h + \beta h}, \quad \text{(A11b)}$$

$$S' = -\frac{1}{\beta}\frac{d}{dz}[C + S]. \quad \text{(A11c)}$$

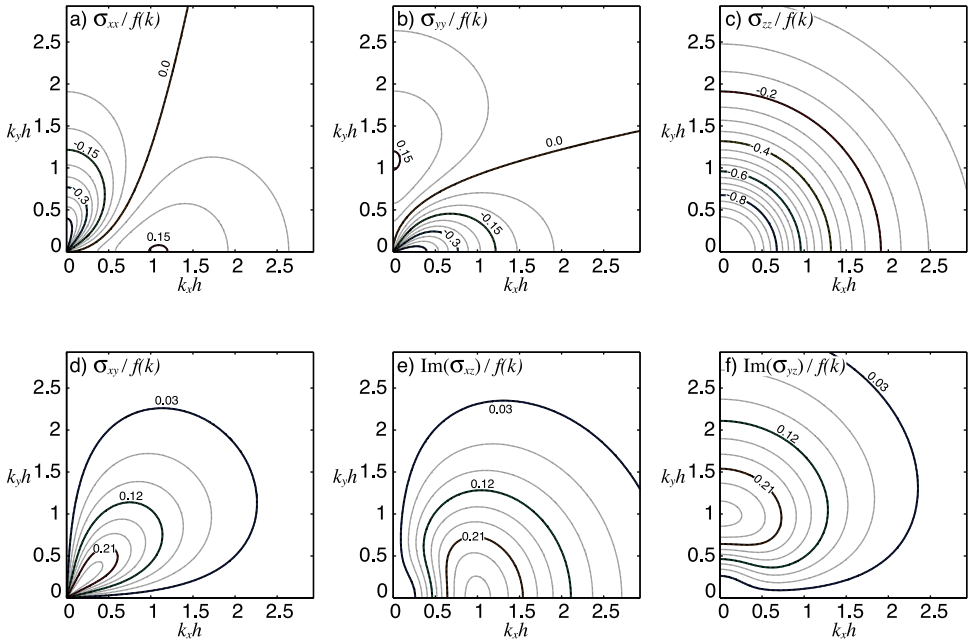

Figure A1. Contours of the Green's functions for each 3-D stress tensor component assuming an Airy-compensated load $g(\vec{k}) = f(\vec{k})$ on an incompressible elastic plate $\nu = 1/2$ at depth $z = h/4$. The dimensionless horizontal wave number is scaled by the plate thickness h, and the dimensionless stress values are scaled by the size of the load $f(\vec{k})$. The Green's functions of the vertical shear stress components σ_{xz} and σ_{yz} are purely imaginary, so the imaginary component is plotted.

In the limit as $\beta \to 0$, the transfer function for the vertical shear stresses S' approaches zero, while the transfer functions for the horizontal shear stress and normal stresses, C and S, both approach 1/2. The long-wavelength stresses therefore become

$$\sigma_{xx} = -f\left(\vec{k}\right)\nu\frac{k_y^2}{\left|\vec{k}\right|^2}, \tag{A12a}$$

$$\sigma_{yy} = -f\left(\vec{k}\right)\nu\frac{k_x^2}{\left|\vec{k}\right|^2}, \tag{A12b}$$

$$\sigma_{xy} = f\left(\vec{k}\right)\nu\frac{k_x k_y}{\left|\vec{k}\right|^2}, \tag{A12c}$$

with the applied load $\sigma_{zz} = -f(\vec{k})$ and the vertical shear stresses $\sigma_{xz} = \sigma_{yz} = 0$. These are the Cartesian stresses for a load within a thin elastic plate [e.g., *Dahlen*, 1981]. On the basis of these three benchmark comparisons, we are confident that the more general 3-D solution is correct.

A4. Minimum Deviatoric Stress in a Loaded Elastic Plate

[43] The solutions of equations (A7a)–(A7f) serve as Green's functions, allowing the full 3-D stress tensor to be computed by a simple convolution in the Fourier domain. We seek the conditions for which the deviatoric stress given by this solution is minimized. The second invariant of the deviatoric stress tensor $\tau_{ij} = \sigma_{ij} - (1/3)\sigma_{kk}$ is given by

$$II_\tau = \frac{1}{6}\left[\left(\sigma_{xx} - \sigma_{yy}\right)^2 + \left(\sigma_{xx} - \sigma_{zz}\right)^2 + \left(\sigma_{yy} - \sigma_{zz}\right)^2\right] + \sigma_{xy}^2 + \sigma_{xz}^2 + \sigma_{yz}^2. \tag{A13}$$

In terms of the transfer functions of equations (A8a)–(A8d) to (A9), this becomes

$$II_\tau = \frac{1}{3}\left[\begin{array}{l} 3\left(f\left(\vec{k}\right)C_f + g\left(\vec{k}\right)C_g\right)^2 - 3\left(f\left(\vec{k}\right)S'_f + g\left(\vec{k}\right)S'_g\right)^2 \\ +\left(f\left(\vec{k}\right)S_f + g\left(\vec{k}\right)S_g\right)^2(1-2\nu)^2 \end{array}\right], \tag{A14}$$

which is minimized when $\nu = 0.5$, corresponding to an incompressible elastic solid. *Dahlen* [1981] similarly showed that in the 2-D case, the second invariant of the deviatoric stress from Airy-compensated topography at midocean ridges was minimized for $\nu = 0.5$, though this was never explicitly stated. Our analysis extends the results of *Dahlen* [1981] to three dimensions. Note that the form of the second invariant is the same as the stress used to define the von Mises yield condition. Therefore, if the material has an elastic-plastic rheology and it has been stressed to its yield strength, then the minimum stress derived here is also the maximum stress that can be maintained in the crust.

[44] The dimensionless Green's functions for an Airy-compensated load $g(\vec{k}) = f(\vec{k})$ on an incompressible elastic plate at depth $z = h/4$ are shown in Figure A1. The wave numbers have been scaled by the plate thickness h and the stress components have been scaled by the applied

load $f(\vec{k})$. In the long-wavelength (zero-wave-number) limit, the vertical shear stresses are zero and the vertical normal stress is the same as the size of the applied load. At this same limit, the horizontal stress components no longer depend on the size of the horizontal radial wave number $|\vec{k}|$, but rather depend on only the relative sizes of the two horizontal wave number components, k_x and k_y, consistent with stress in a thin elastic plate. In the short-wavelength (infinite-wave-number) limit, all stress components go to zero.

[45] The Fortran code to calculate the 3-D stress field that is due to an arbitrary surface topography load is provided at the following ftp location: ftp://topex.ucsd.edu/pub/chile_topo_stress.

[46] **Acknowledgments.** We thank Martin Mai for providing his code to validate our stress drop calculations. We thank the associate editor and two anonymous reviewers for their comments on this paper. This research was supported by NASA Geodetic Imaging NNX09AD12G, the NASA Earth and Space Science Fellowship Program, and NSF EAR0811772.

References

Allmann, B. P., and P. M. Shearer (2009), Global variations of stress drop for moderate to large earthquakes, *J. Geophys. Res.*, *114*, B01310, doi:10.1029/2008JB005821.

Andrews, D. J. (1980), A stochastic fault model: 1. Static case, *J. Geophys. Res.*, *85*(B7), 3867–3877, doi:10.1029/JB085iB07p03867.

Bamler, R., and M. Eineder (1996), ScanSAR processing using standard high precision SAR algorithms, *IEEE Trans. Geosci. Remote Sens.*, *34* (1), 212–218, doi:10.1109/36.481905.

Becker, J. J., et al. (2009), Global bathymetry and elevation data at 30 arc seconds resolution: SRTM30_PLUS, *Mar. Geod.*, *32*(4), 355–371, doi:10.1080/01490410903297766.

Billen, M., E. Cowgill, and E. Buer (2007), Determination of fault friction from reactivation of abyssal-hill faults in subduction zones, *Geology*, *35* (9), 819–822, doi:10.1130/G23847A.1.

Boussinesq, J. (1885), *Application des Potentiels a l'Etude de l'Equilibre et du Mouvement des Solides Elastiques*, 508 pp., Gauthier-Villars, Paris.

Brooks, B. A., M. Bevis, R. Smalley Jr., E. Kendrick, R. Manceda, E. Lauria, R. Maturana, and M. Araujo (2003), Crustal motion in the Southern Andes (26°–36°S): Do the Andes behave like a microplate?, *Geochem. Geophys. Geosyst.*, *4*(10), 1085, doi:10.1029/2003GC000505.

Byerlee, J. (1978), Friction of rocks, *Pure Appl. Geophys.*, *116*(4–5), 615–626, doi:10.1007/BF00876528.

Cattin, R., H. Lyon-Caen, and J. Chéry (1997), Quantification of interplate coupling in subduction zones and forearc topography, *Geophys. Res. Lett.*, *24*(13), 1563–1566, doi:10.1029/97GL01550.

Dahlen, F. A. (1981), Isostasy and the ambient state of stress in the oceanic lithosphere, *J. Geophys. Res.*, *86*(B9), 7801–7807, doi:10.1029/JB086iB09p07801.

Dahlen, F. A. (1990), Critical taper model of fold-and-thrust belts and accretionary wedges, *Annu. Rev. Earth Planet. Sci.*, *18*, 55–99, doi:10.1146/annurev.ea.18.050190.000415.

Delouis, B., J. M. Nocquet, and M. Vallée (2010), Slip distribution of the February 27, 2010 Mw = 8.8 Maule Earthquake, central Chile, from static and high-rate GPS, InSAR, and broadband teleseismic data, *Geophys. Res. Lett.*, *37*, L17305, doi:10.1029/2010GL043899.

Fialko, Y. (2004), Probing the mechanical properties of seismically active crust with space geodesy: Study of the coseismic deformation due to the 1992 M_w 7.3 Landers (southern California) earthquake, *J. Geophys. Res.*, *109*, B03307, doi:10.1029/2003JB002756.

Hardebeck, J. L., and A. Aron (2009), Earthquake stress drops and inferred fault strength on the Hayward Fault, east San Francisco Bay, California, *Bull. Seismol. Soc. Am.*, *99*(3), 1801–1814, doi:10.1785/0120080242.

Hardebeck, J. L., and A. J. Michael (2004), Stress orientations at intermediate angles to the San Andreas Fault, California, *J. Geophys. Res.*, *109*, B11303, doi:10.1029/2004JB003239.

Jackson, J., D. McKenzie, K. Priestley, and B. Emmerson (2008), New views on the structure and rheology of the lithosphere, *J. Geol. Soc.*, *165*(2), 453–465, doi:10.1144/0016-76492007-109.

Kendrick, E., M. Bevis, R. Smalley, B. Brooks, R. B. Vargas, E. Lauria, and L. P. S. Fortes (2003), The Nazca South America Euler vector and its rate of change, *J. South Am. Earth Sci.*, *16*(2), 125–131, doi:10.1016/S0895-9811(03)00028-2.

Lamb, S. (2006), Shear stresses on megathrusts: Implications for mountain building behind subduction zones, *J. Geophys. Res.*, *111*, B07401, doi:10.1029/2005JB003916.

Lamb, S., and P. Davis (2003), Cenozoic climate change as a possible cause for the rise of the Andes, *Nature*, *425*(6960), 792–797, doi:10.1038/nature02049.

Lay, T., C. J. Ammon, H. Kanamori, K. D. Koper, O. Sufri, and A. R. Hutko (2010), Teleseismic inversion for rupture process of the 27 February 2010 Chile (M_w 8.8) earthquake, *Geophys. Res. Lett.*, *37*, L13301, doi:10.1029/2010GL043379.

Leyton, F., J. Ruiz, J. Campos, and E. Kausel (2009), Intraplate and interplate earthquakes in Chilean subduction zone: A theoretical and observational comparison, *Phys. Earth Planet. Inter.*, *175*(1–2), 37–46, doi:10.1016/j.pepi.2008.03.017.

Lloyd, S., S. van der Lee, G. S. Franca, M. Assumpcao, and M. Feng (2010), Moho map of South America from receiver functions and surface waves, *J. Geophys. Res.*, *115*, B11315, doi:10.1029/2009JB006829.

Lorito, S., F. Romano, S. Atzori, X. Tong, A. Avallone, J. McCloskey, M. Cocco, E. Boschi, and A. Piatanesi (2011), Limited overlap between the seismic gap and coseismic slip of the great 2010 Chile earthquake, *Nat. Geosci.*, *4*, 173–177, doi:10.1038/ngeo1073.

Love, A. E. H. (1929), The stress produced in a semi-infinite solid by pressure on part of the boundary, *Proc. R. Soc. London Ser. A*, *228*, 377–420.

Luttrell, K., and D. Sandwell (2010), Ocean loading effects on stress at near shore plate boundary fault systems, *J. Geophys. Res.*, *115*, B08411, doi:10.1029/2009JB006541.

Luttrell, K., D. Sandwell, B. Smith-Konter, B. Bills, and Y. Bock (2007), Modulation of the earthquake cycle at the southern San Andreas fault by lake loading, *J. Geophys. Res.*, *112*, B08411, doi:10.1029/2006JB004752.

Madariaga, R., M. Metois, C. Vigny, and J. Campos (2010), Central Chile finally breaks, *Science*, *328*(5975), 181–182, doi:10.1126/science.1189197.

Moreno, M., M. Rosenau, and O. Oncken (2010) 2010 Maule earthquake slip correlates with pre-seismic locking of Andean subduction zone, *Nature*, *467*(7312), 198–202, doi:10.1038/nature09349.

Okada, Y. (1985), Surface deformation due to shear and tensile faults in a half-space, *Bull. Seismol. Soc. Am.*, *75*(4), 1135–1154.

Okada, Y. (1992), Internal deformation due to shear and tensile faults in a half-space, *Bull. Seismol. Soc. Am.*, *82*(2), 1018–1040.

Ortiz, A. B., and H. Zebker (2007), ScanSAR-to-stripmap mode interferometry processing using ENVISAT/ASAR data, *IEEE Trans. Geosci. Remote Sens.*, *45*(11), 3468–3480, doi:10.1109/TGRS.2007.895970.

Pavlis, N. K., S. A. Holmes, S. C. Kenyon, and J. K. Factor (2008), An Earth gravitational model to degree 2160, paper presented at European Geosciences Union General Assembly, Vienna, 13–18 April.

Pollitz, F., et al. (2011), Coseismic slip distribution of the February 27, 2010 Mw 8.8 Maule, Chile earthquake, *Geophys. Res. Lett.*, *38*, L09309, doi:10.1029/2011GL047065.

Ripperger, J., and P. M. Mai (2004), Fast computation of static stress changes on 2D faults from final slip distributions, *Geophys. Res. Lett.*, *31*, L18610, doi:10.1029/2004GL020594.

Sandwell, D. T., and W. H. F. Smith (2009), Global marine gravity from retracked Geosat and ERS-1 altimetry: Ridge segmentation versus spreading rate, *J. Geophys. Res.*, *114*, B01411, doi:10.1029/2008JB006008.

Sandwell, D. T., D. Myer, R. Mellors, M. Shimada, B. Brooks, and J. Foster (2008), Accuracy and resolution of ALOS interferometry: Vector deformation maps of the Father's Day intrusion at Kilauea, *IEEE Trans. Geosci. Remote Sens.*, *46*(11), 3524–3534, doi:10.1109/TGRS.2008.2000634.

Scholz, C. H. (2000), Evidence for a strong San Andreas fault, *Geology*, *28* (2), 163–166, doi:10.1130/0091-7613(2000)28<163:EFASSA>2.0.CO;2.

Seno, T. (2009), Determination of the pore fluid pressure ratio at seismogenic megathrusts in subduction zones: Implications for strength of asperities and Andean-type mountain building, *J. Geophys. Res.*, *114*, B05405, doi:10.1029/2008JB005889.

Shimada, M., T. Tadono, and A. Rosenqvist (2010), Advanced Land Observing Satellite (ALOS) and monitoring global environmental change, *Proc. IEEE*, *98*(5), 780–799, doi:10.1109/JPROC.2009.2033724.

Sick, C., et al. (2006), Seismic images of accretive and erosive subduction zones from the Chilean Margin, in *The Andes: Frontiers in Earth Sciences*, edited by O. Oncken et al., pp. 147–169, Springer, Berlin.

Smith, B., and D. Sandwell (2004), A three-dimensional semianalytic viscoelastic model for time-dependent analyses of the earthquake cycle, *J. Geophys. Res.*, *109*, B12401, doi:10.1029/2004JB003185.

Steketee, J. A. (1958), On Volterra's dislocations in a semi-infinite elastic medium, *Can. J. Phys.*, *36*, 192–205, doi:10.1139/p58-024.

Tassara, A. (2010), Control of forearc density structure on megathrust shear strength along the Chilean subduction zone, *Tectonophysics*, *495*(1–2), 34–47, doi:10.1016/j.tecto.2010.06.004.

Tong, X., D. T. Sandwell, and Y. Fialko (2010a), Coseismic slip model of the 2008 Wenchuan earthquake derived from joint inversion of interferometric synthetic aperture radar, GPS, and field data, *J. Geophys. Res.*, *115*, B04314, doi:10.1029/2009JB006625.

Tong, X., et al. (2010b), The 2010 Maule, Chile earthquake: Downdip rupture limit revealed by space geodesy, *Geophys. Res. Lett.*, *37*, L24311, doi:10.1029/2010GL045805.

Vigny, C., et al. (2011), The 2010 M_w 8.8 Maule megathrust earthquake of central Chile, monitored by GPS, *Science*, *332*(6036), 1417–1421, doi:10.1126/science.1204132.

Yuan, X., S. V. Sobolev, and R. Kind (2002), Moho topography in the central Andes and its geodynamic implications, *Earth Planet. Sci. Lett.*, *199* (3–4), 389–402, doi:10.1016/S0012-821X(02)00589-7.

Zhong, S. J., and M. Gurnis (1994), Controls on trench topography from dynamic models of subducted slabs, *J. Geophys. Res.*, *99*(B8), 15,683–15,695, doi:10.1029/94JB00809.

Zoback, M. D. (2000), Strength of the San Andreas, *Nature*, *405*(6782), 31–32, doi:10.1038/35011181.

Zoback, M. L. (1992), First and second-order patterns of stress in the lithosphere: The World Stress Map project, *J. Geophys. Res.*, *97*(B8), 11,703–11,728, doi:10.1029/92JB00132.

M. Bevis, School of Earth Sciences, Ohio State University, 125 S. Oval Mall, Columbus, OH 43210, USA. (mbevis@osu.edu)

B. Brooks, School of Ocean and Earth Science and Technology, University of Hawai'i at Manoa, 1680 East-West Rd., Honolulu, HI 96822, USA. (bbrooks@hawaii.edu)

K. Luttrell, Volcano Science Center, U.S. Geological Survey, 345 Middlefield Rd., MS 910, Menlo Park, CA 94025, USA. (kluttrell@usgs.gov)

D. Sandwell and X. Tong, Scripps Institution of Oceanography, University of California, San Diego, 9500 Gilman Dr., MS 225, La Jolla, CA 92093, USA. (dsandwell@ucsd.edu; xitong@ucsd.edu)